Journal Pre-proof

Experimental investigation of catalan vault structures based on earthen materials

M. Franciosi, V. Savino, L. Lanzoni, A.M. Tarantino, M. Viviani

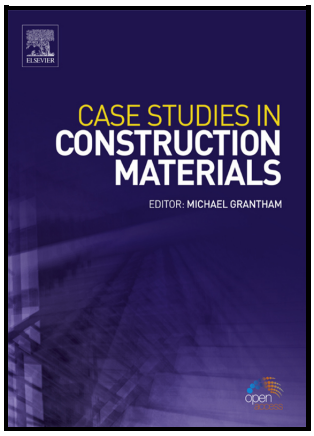

PII: S2214-5095(24)00716-2

DOI: https://doi.org/10.1016/j.cscm.2024.e03565

Reference: CSCM3565

To appear in: *Case Studies in Construction Materials*

Received date: 30 April 2024
Revised date: 20 June 2024
Accepted date: 23 July 2024

Please cite this article as: M. Franciosi, V. Savino, L. Lanzoni, A.M. Tarantino and M. Viviani, Experimental investigation of catalan vault structures based on earthen materials, *Case Studies in Construction Materials,* (2024) doi:https://doi.org/10.1016/j.cscm.2024.e03565

Experimental investigation of catalan vault structures based on earthen materials

M. Franciosi [1], V. Savino [1], L. Lanzoni [2], A. M. Tarantino [2], M. Viviani [1]

[1] HEIG-VD/HES-SO - University of Applied Sciences and Arts Western Switzerland, Route de Cheseaux 1, CH-1401 Yverdon, Switzerland

[2] Department of Engineering "Enzo Ferrari", University of Modena and Reggio Emilia, 41125 Modena, Italy

Abstract

The Catalan vaulting have succeeded in reducing reliance on support centers, resulting in lowered costs and expedited construction processes. This research advances the study of Catalan vaulting by exploring innovative, environmentally friendly earth-based materials. The study conducts a comprehensive comparative analysis of load-bearing behaviors across distinct vault elements: those fabricated from terracotta, raw-earth tiles, and shot-earth. Constructed and tested at a 4-meter span, full-scale vault specimens are subjected to varying distributed load configuration, followed by rupture testing employing a linear load at a quarter of the span. Experimental evidence, corroborated by FE results, indicates that both terracotta and raw earth tile vaults offer commendable performance, yet their failure loads are surpassed by vaults constructed using shot-earth. Therefore, shot-earth emerges as a sustainable alternative for constructing vault elements. Furthermore, the study demonstrates that incorporating reinforcement within shot-earth vaults increases their strength and ductility.

Keywords: Earthen materials, Modern building materials, Sustainable constructions, Catalan Vault, FE analyses

Nomenclature

SE	Shot-earth
ER	Ecorasilla masonry
RM	Rasilla terracotta masonry
V-SE	Vault made of shot-earth
V-ER	Vault made of Ecorasilla masonry
V-RM	Vault made of Rasilla terracotta masonry
C1	Uniformly distributed load condition
C2	Asymmetric distributed load condition
C3	Asymmetric line load condition
RH	Relative humidity
GFRP	Glass fiber-reinforced polymer
W-ER-I	Ecorasilla masonry wall i-th samples
W-SE-i	Shot-earth wall i-th samples
W-RM-i	Rasilla terracotta masonry wall i-th samples
F-RM-i	Rasilla terracotta masonry prism i-th samples
$f_{c,max}$	Maximum compression strength
EM	Elastic modulus
LVDT	Linear Variable Displacement Transducer
A_c	Wall compressed area
F_{max}	Maximum load recorded during the axial compression test
R	Loading rate in the three-point bending test

d_1 and d_2	Lateral dimensions of the cross-section of the F-RM-i
s	Constant rate of stress
l	Distance between supporting rollers
$f_{ct,fl}$	Flexural strength
F	Maximum load recorded during the three-point bending test
δ(F)	Midspan displacement at F
L_V	Total length of the vault
L_P	Shorter distance between the two vault supports
b	Width of the vaults
h	Thickness of the vaults
R_V	Radius of the curved line of the vaults
K	Equivalent stiffness of the chain system
E_s	Elastic modulus of the steel chains
A_{sc}	Cross-sectional area of a single chain
l_s	Length of the horizontal chains
b_s	Distance between the two horizontal chains
A_s	Cross-sectional area of the steel reinforcement
ø	Rebar diameter
V-ER-Ci	Experimental deflections measured for the V-ER under the Ci-th loading condition
V-SE-Ci	Experimental deflections measured for the V-SE under the Ci-th loading condition
V-RM-Ci	Experimental deflections measured for the V-RM under the Ci-th loading condition
V-ER-FEM-Ci	Deflections calculated for the V-ER under the Ci-th loading condition using the FE model
V-SE-FEM-Ci	Deflections calculated for the V-SE under the Ci-th loading condition using the FE model
V-RM-FEM-Ci	Deflections calculated for the V-RM under the Ci-th loading condition using the FE model
FVSE1	Load that triggers the formation of the first plastic hinge in V-SE

1. Introduction

Vaults and domes are shell structures created through the translation and rotation of arches, respectively. Depending on their shape, basically three main types of vaults can be distinguished: (i) barrel vaults, (ii) cross vaults, and (iii) rib vaults [1]. Barrel vaults are formed by a simple longitudinal translation of an arch, as shown in Fig. 1a. Their structural behavior depends on the ratio between the span and the width of the transverse chord. Cross vaults are created by the intersection of two-barrel vaults at a right angle, as illustrated in Fig. 1b. On the other hand, ribbed vaults are achieved by intersecting two-pointed barrel vaults, as depicted in Fig. 1c. The ribs function as a supporting skeleton and are a key characteristic of Gothic vaults.

Dome shell structures, on the other hand, are created through the rotation of an arch. In Fig. 2a, the unitary forces for an infinitesimal portion of one of the most famous domes, the hemispherical dome, are presented. When subjected to self-weight loads under membrane behavior conditions, the distribution of axial forces along the meridians and rings, as a function of colatitude (referred to hereafter as "φ"), indicates that the meridians are in compression. However, beyond a specific angle ($\varphi > 52°$), the rings change their condition from compression to a tension state, as depicted in Fig. 2b.

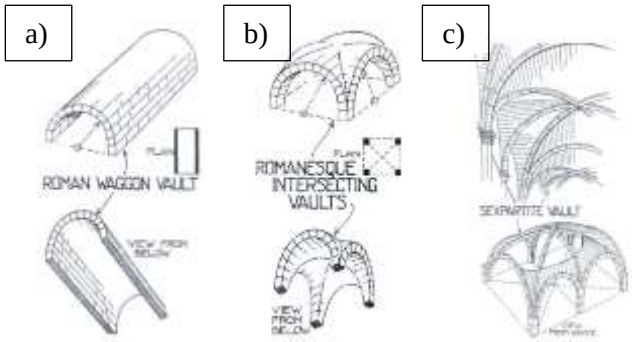

Fig. 1. a) Barrel vault, b) Cross vault, c) Ribs vault (from [2]).

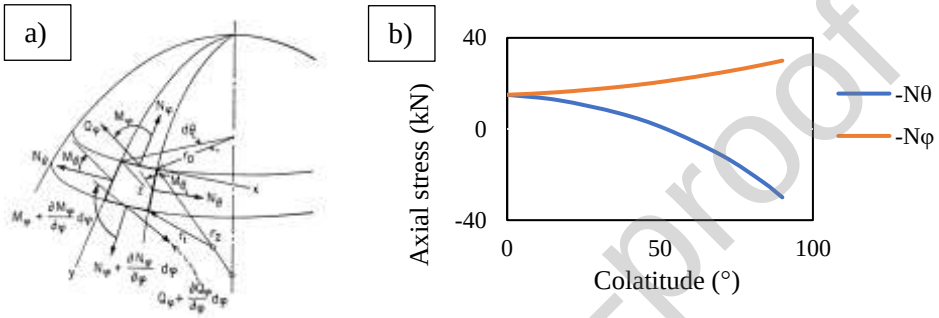

Fig. 2. a) Resultant forces in a hemispherical dome infinitesimal portion (from [3]), b) Axial forces along the meridians (N_φ) and rings (N_θ) for a hemispherical dome subjected to self-weight load under membrane regime.

The earliest arched structures, dating back to 2000 BC [4], were constructed using pressed earth blocks, commonly known as "adobe," which represent one of the oldest vernacular building systems [5]. Two of the most significant examples include the Beehive house (Fig. 3a) and Taq Kasra, located in ancient Persia, now Iraq (Fig. 3b). Taq Kasra is particularly noteworthy as an inverse funicular structure, and it still holds the distinction of being the largest brick vault structure in the world.

Fig. 3. a) Beehive houses sited in Harran (Turkey) (from [6]), b) Taq Kasra sited in Iraq (from [7]).

The Persian architecture was also characterized by bulb domes that have lower thickness compared to the hemispherical ones. Concerning vaulting structure, five principal technologies have been developed over the centuries: (i) Roman vaulting (centering), (ii) Corbelling, (iii) Nubian vaulting, (iv) Gothic vaulting, and (v) Catalan vaulting. The roman vaulting technique is based on concept of centering in which the bricks are arranged in a radial direction and until the keystone is positioned the arch does not support its self-weight and therefore formwork is needed during the construction phase. In the corbelling

technique, the disposition of the masonry elements layers is made in a way that the projection of the mass center remains at the base of the system ensuring stability without formwork. Discovered in ancient Nubia the Nubian vaulting techniques used a vertical surface as a backrest to lead inclined courses of brick. Another main principle of Nubian vaulting technique is that the cross section follows the catenary shape. In the Gothic vaults, the ribs are the main structural element, and the gaps were filled with stone or brick masonry. The Catalan vaulting technique was developed in Catalogna, and thanks to Gustavino, it has been also extensively used in America in the 19th and 20th centuries. The Catalan vaulting technique is based on the use of lightweight bricks and quick-setting mortar that bonds the bricks together [8]. This allows to construct without formwork. The binder used for the first layer is often a plaster paste material, in this way the first layer acts as a center for the successive ones. Lime mortar is used for successive layers and this allows improving the strength and the loadbearing capacity of the vault [9]. These (usually variable between one and three) are laid by rotating the orientation of the bricks of 45° [10].

These kinds of structures characterized mainly by a compressive behavior can be divided in two groups based on their shape: (i) active form systems, and (ii) surface form systems. The first ones are characterized by a flexible shape that follow the catenary. This geometry is not appropriate for a barrel vault due to the stress in the support being 2.5 times higher than that would occur with a circular shape [11]. The surface form systems are shell structures that support the load with a combination of bending and membrane actions [12]. The membrane theory gives a satisfactory result for the portions of vault that are a considerable distance from the edges, but the boundary conditions are not satisfied. Therefore, the membrane theory can be used as an approximate solution that have to be combined with more elaborate bending theories that permit to satisfy the boundary conditions at the edges [3]. If the rectilinear edges are simply supported and the other two edges are free, a solution similar to that of M. Lévy's method can be applied [13]. Nowadays the evaluation of the stress due to different load combinations is commonly performed via finite element methods (FEMs) and the masonry is modeled as a continuous material with defined elastic properties [14].

Traditionally, materials such as adobe (mudbrick), clay (firebrick), and stone were commonly used to construct vaults [1]. However, over time, other technologies such as concrete and traditional masonry have also been utilized for their economic and performance advantages. In recent years, the increasing interest in alternative ecological solutions, newer materials, including earth-based materials, have gained popularity. To evaluate the performance and behavior of these materials in real-scale vaults, an experimental campaign has been conducted. This campaign aims to investigate the response of three distinct vault types both in elastic and failure domains. Specifically, two of the materials under examination are earth-based materials: Shot-earth (labeled hereafter "SE") and Ecorasilla masonry (labeled hereafter "ER"), while the third is rasilla terracotta masonry (labeled hereafter "RM"). The respective vault samples hereinafter will be labeled "V-SE", "V-ER" and "V-RM". The thin terracotta tiles named "rasilla" were the bricks generally used for Catalan vaults. The ER due to the low amount

of cement used on it as stabilizer is presented here as an ecological version of “rasilla”. The term "Ecorasilla" denotes a thin tile primarily consisting of excavated earth from construction sites, water, and a minimal amount of stabilizer, produced using a compaction technique [15]. The ER characteristic are reported in detail in [10]. SE is a new class of earthen construction materials obtained by high-speed projection composed by: grinded earth, aggregates (size 0-8 mm), water and, if needed, a low amount of stabilizer can be added. The latter can be hydraulic of hydrated lime, plaster, cement or geopolymer. Numerous works about the mechanical, thermal and hygrothermal properties of SE can be found in Literature [16–21]. The RM is held as a comparison with the other two more ecological technologies.

The aim of this study is to highlight the feasibility of utilizing earth-based materials as a sustainable approach for constructing Catalan vaults, analyzed from a structural perspective. This is achieved through the construction of three vaults in ER, SE, and RM respectively. A comparison is made by measuring displacements and resistances under different loading conditions, including both serviceability and ultimate failure states. For the service load, two loading patterns are considered: (i) uniformly distributed load (referred to as “C1”), and (ii) asymmetric distributed load (referred to as “C2”). Additionally, severe asymmetrical line load conditions (referred to as “C3”) are examined at failure. A constant comparison between experimental results and finite element FE models is conducted to assess the predictive capability of this system using simplified FE models. Specifically, at failure, the FE results are analyzed in conjunction with axial force – bending moment interaction domains for specific cross-sections to predict both the ultimate load and failure mode.

2. Materials and methods

2.1. Ecorasillas masonry (ER)

ER tiles mixture proportions are: 2 volume of grinded earth, 1 volume of river sand (size 0-4 mm) and 12% by weight of stabilizer (Portland cement CEM I 42.5 N). The mix design is based on what is used in [10]. The cement content is equivalent to that found in other earth-based materials, such as pressed earth and rammed earth [20,22]. This enhances sustainability by achieving a cement content similar to that of low-strength concrete.

The earth at hand is taken from the excavation site at Ault (France). As the water content is a key aspect for the earthen construction [23,24] an 8% in water mass is added in accordance to Literature to reach the optimum moisture content [25–29]. All the compounds are mixed together in a standard concrete mixer for a couple of minutes. After that, the fresh mixture is compacted via hydraulic static device inside a prismatic formwork at the pressure of 0.01 MPa allowing to obtain tiles of 20 x 130 x 260 mm^3. The ER tiles after the mold extraction are cured under controlled condition at 20 ± 2 °C of temperature and 55 ± 10% of RH for one week and then let dry for three weeks. The same layer tiles arrangement used for the Catalan vaults’ construction is adopted for the realization of both walls and vaults. The three layers are disposed as sketched in Fig. 4a. As the first layer of ER tiles and mortar plays a formwork

role for the superior ones, a special mortar is used to bond the first layer. For all the others a M5 Portland cement-based mortar is used. A glass-fiber-reinforced polymer (labeled hereafter "GFRP") mesh [30] is embedded between the second and third layer to reinforce the mortar, see Fig. 4a. The final thickness of ER masonry reaches approximately 11.5 cm.

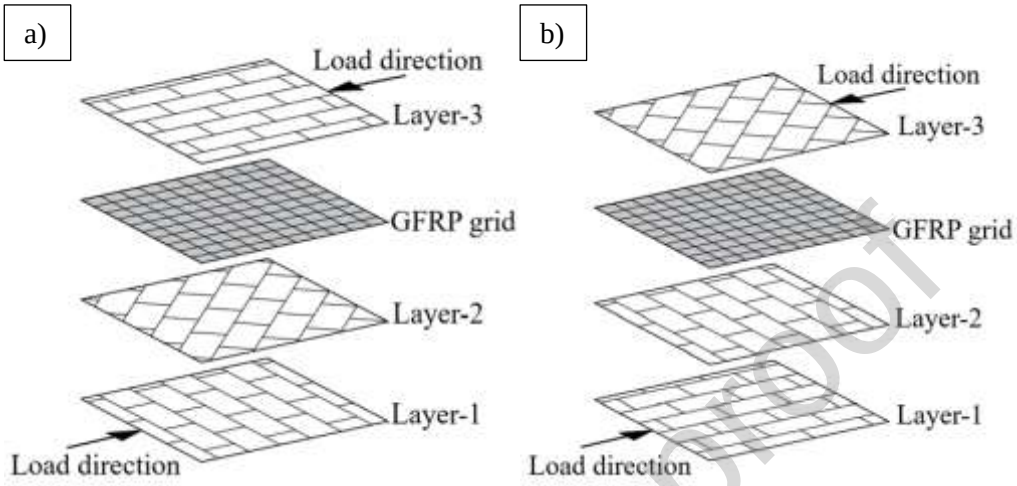

Fig. 4. Layer order of bricks in: a) ER, b) RM. The load direction is representative only for the axial compression test of wall.

2.2. Shot-earth (SE)

The SE studied in this work consists of stabilized soil with cement, aggregates, and water. The earth is collected from the excavation site in Moudon (Switzerland), after removing the topmost layer (25 – 50 cm) as it contains organic material. In accordance with the EN 12620 standard [31], a commercially available aggregate with a particle size of 0 to 8 mm for concrete is used. The stabilizer used is the Portland cement (CEM I 42.5 N) which complies with the requirements of the EN 197-1 standard [32]. The dry mixture proportion adopted here is 7 volumes of soil, 7 of sand and 2 of cement. SE is obtained via a projection process at high speed. A purpose-designed machine permits, before the projection, to mix the dry parts homogeneously. During the mixing stage, 3% of water (by volume) is added just to promote cohesion and the hydration of the stabilizer. Further information about the projection process and machine characteristics are reported in [18].

2.3. Rasillas masonry (RM)

In RM, modern terracotta rasilla tiles measuring 30 x 180 x 240 mm³ are used. The 'rasilla' tiles are manufactured in compliance with UNI EN 771-1:2011 [33] standard by a local producer. The RM differs from the ER only in terms of layer orientation, while maintaining the same mortars usage and GFRP location, as shown in Fig. 4b. The final thickness of RM is approximately 12 cm. The thickness variability observed is considered acceptable as it depends on the consistency of the mortar at the time of its placement and the operator's ability.

3. Preliminary investigations about material properties

3.1. Specimens

In order to develop analytical and/or numerical mechanical models capable of predicting vault behavior, a preliminary investigation was conducted to assess the main material properties. This involved conducting axial compression tests on wall-like samples and evaluating the (indirect) tensile strength of RM through three-point bending tests. For the other two materials, this parameter was obtained from existing Literature [10,18].

The manufacturing and curing processes for these samples are identical to those described for the vaults, as outlined in Section 4.1. A summary of the specimen sizes and the types of tests conducted is provided in Table 1.

Table 1
Experimental tests carried out during the preliminary investigation of the materials characteristics.

Specimens	Label	Number of specimens	Test	Regulation
ER wall 1x1x0.115 m^3	W-ER-i	2	Axial compression tests	[10,34,35]
SE wall 0.8x0.8x0.1 m^3	W-SE-i	2	Axial compression tests	[10,34,35]
RM wall 0.8x0.8x0.14 m^3	W-RM-i	3	Axial compression tests	[10,34,35]
RM prism 0.24x0.118x0.11 m^3	F-RM-i	3	3-point bending test	[36]

i: Sample number

3.2. Axial compression test of wall

To determine the maximum compression strength (referred to as "$f_{c,max}$") and the elastic modulus (referred to as "EM") for the various materials analyzed in this study, tests were conducted on different walls in an axial compression configuration, as illustrated in Fig. 5. A load frame was assembled and equipped with two 300 kN servo-hydraulic actuators intended to apply a constant load by placing a steel beam between them. To minimize surface irregularities, a thin layer of quick-setting and hardening cement was applied at the bottom and top of the wall. As depicted in Fig. 5, a system of LVDTs with an accuracy of ±0.002 mm and a gauge length of 250 mm was affixed to the wall's surface to measure both vertical and horizontal strains. Six LVDTs (three on each side) were positioned. For clarity, the two sides of each wall or specimen will be referred to as "sideA" and "sideB."

The load was applied at a deflection rate of 0.5 mm/min [34,35]. Data were continuously recorded using a digital acquisition system at a sampling frequency of 10 Hz. The elastic modulus (EM) was estimated through linear regression on the stress-vertical strain curve within the range of 5% to 30% of $f_{c,max}$. The $f_{c,max}$ is calculated according to Eq. (1),

$$f_{c,max} = \frac{F_{max}}{A_c}, \quad (1)$$

where F_{max} is the maximum load registered (N) and A_c is the wall compressed area (mm^2).

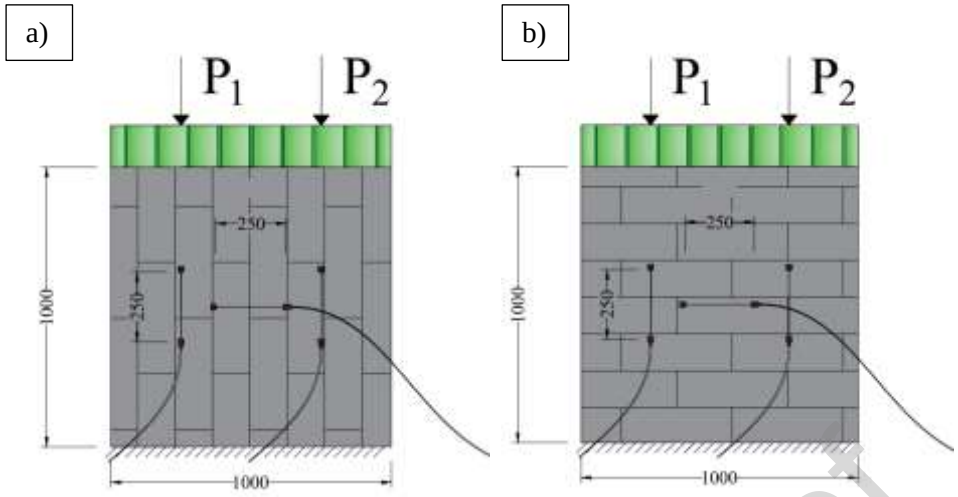

Fig. 5. Load pattern for axial compression test on walls and LVDT's arrangement for a) W-ER-sideA and b) W-ER-sideB (dimensions in mm).

Fig. 6 displays various crack patterns observed during the axial compression tests. The findings presented in Table 2, which include $f_{c,max}$ and EM values, lead to the following conclusions: (i) all the examined materials are suitable for use in load-bearing wall applications, (ii) materials with the highest $f_{c,max}$ values also exhibit greater stiffness, and (iii) the results for SE materials align with those previously reported in the Literature [18], thereby confirming the repeatability of material properties while maintaining a consistent mix design.

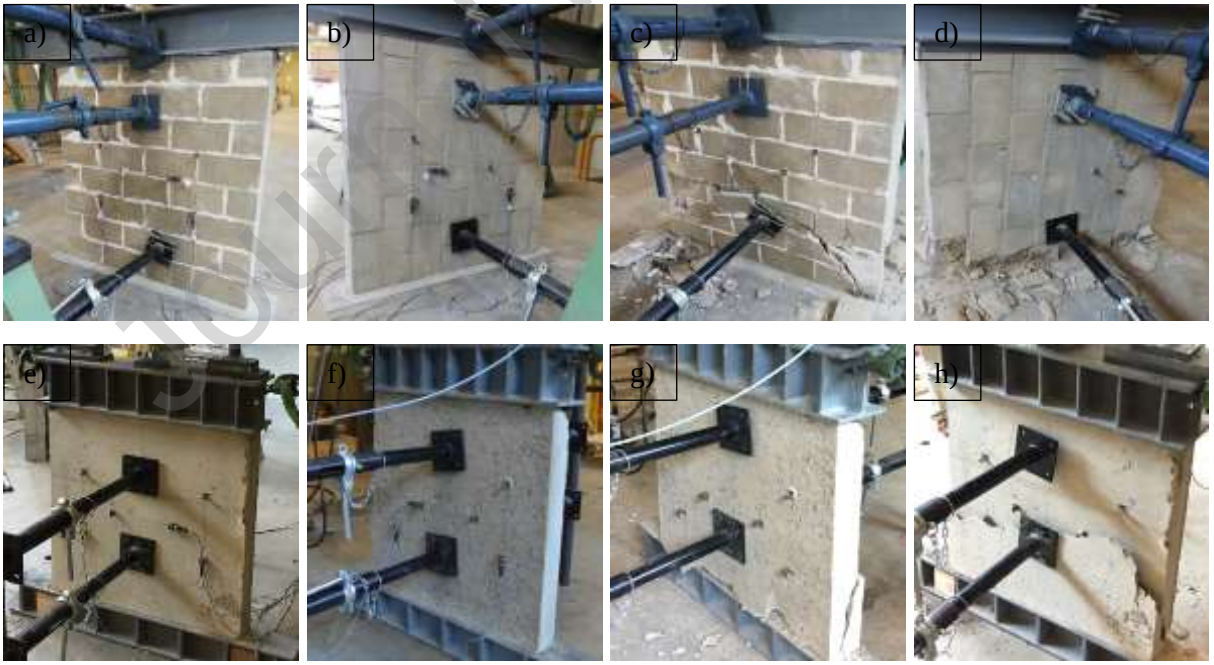

Fig. 6. Wall before the compression test: a) W-ER-sideA, b) W-ER-sideB, e) W-SE-sideA, f) W-SE-sideB, i) W-RM-sideA, j) W-RM-sideB. Wall after the compression test: c) W-ER-sideA, d) W-ER-sideB, g) W-SE-sideA, h) W-SE-sideB, k) W-RM-sideA, l) W-RM-sideB.

Table 2
Results provided by the wall axial compression tests.

Specimens	$f_{c,max}$ (MPa)	EM (MPa)
W-ER-1	6.12	4301
W-ER-2	6.91	5624
Avg.	**6.51 ± 0.56**	**4962 ± 936**
W-SE-1	11.70	13311
W-SE-2	10.10	12684
Avg.	**10.90 ± 1.13**	**12998 ± 443**
W-RM-1	8.14	7203
W-RM-2	6.78	7281
W-RM-3	8.09	8435
Avg.	**7.67 ± 0.77**	**7640 ± 690**

$f_{c,max}$: ultimate compression strength;
EM: Elastic moment evaluated between 5% and 30% of $f_{c,max}$.

3.3. Three-point loading bending test

The loading system utilizes a roller positioned at the center with respect to the two lower supports, thus creating a three-point bending load configuration, as illustrated in Fig. 7. An LVDT is vertically placed at the intrados fiber of the beam to measure the midspan displacement. Data is continuously recorded using a digital acquisition system at a frequency of 10 Hz.

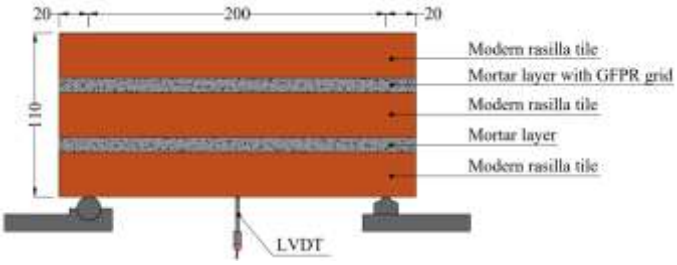

Fig. 7. Load pattern for three-point loading bending test.

According to EN 12390-5:2019, the tests were conducted at a consistent loading rate of 238 N/s, as calculated in Eq. (2), until failure occurred:

$$R = \frac{2 \times d_1 \times d_2^2 \times s}{3 \times l} \quad (2)$$

where R is the loading rate (N/s), d_1 and d_2 are the lateral dimensions of the cross-section (mm), s is the constant rate of stress (0.05 MPa/s) and l is the distance between the supporting rollers (mm). The applied preload was 0.5 kN.

The results of the F-RM tests are represented graphically by load-midspan deflection curves, as seen in Fig. 8a. The flexural performance of the F-RM is summarized in Table 3, with the flexural strength calculated using Eq. (3).

$$f_{ct,fl} = \frac{3 \times F \times l}{2 \times d_1 \times d_2^2} \quad (3)$$

Where $f_{ct,fl}$ is the flexural strength (MPa), F is the maximum load (N), l is the distance between the supporting rollers (mm) and d_1 and d_2 are the lateral dimensions of the cross-section (mm). The F-RM exhibited an elastic behavior until the first crack appeared, as shown in Fig. 8. Subsequently, a sudden failure occurred.

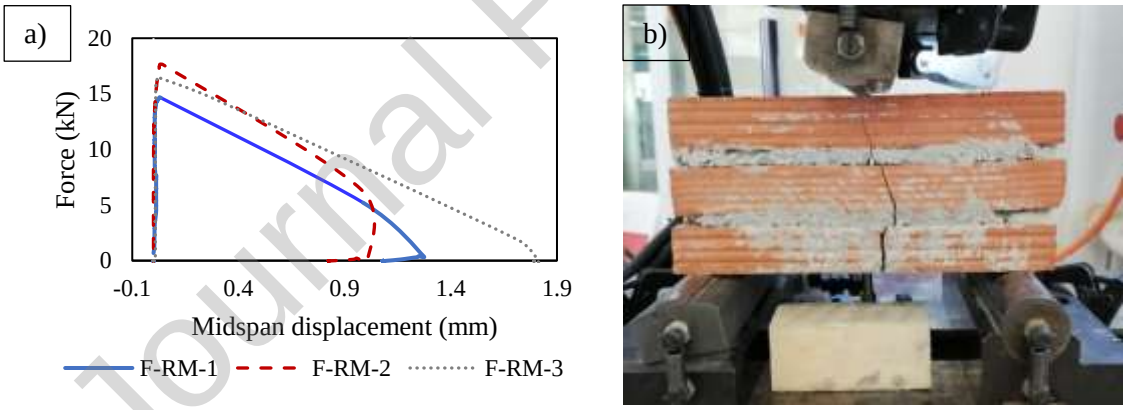

Fig. 8. a) Load-midspan deflection response; b) Crack pattern of F-RM.

Table 3
Three-point loading bending test experimental results.

Specimens	F (kN)	δ(F) (mm)	$f_{ct,fl}$ (MPa)
F-RM-1	14.76	0.034	3.20
F-RM-2	17.74	0.042	3.49
F-RM-3	16.66	0.026	3.55
Avg.	**16.39 ± 1.51**	**0.034 ± 0.008**	**3.41 ± 0.18**

F_RM-i: identification label for rasilla masonry samples;
F: ultimate load;
δ(F): midspan deflection at ultimate load;
$f_{ct,fl}$: flexural strength.

4. Vaults

4.1. Fabrication and curing of the vaults

For this testing campaign, three vaults were manufactured, each representing a different material type as described in Section 2. The geometric parameters of these vaults are listed in Table 4. The vaults are supported on two reinforced concrete blocks designed to replicate realistic boundary conditions. These concrete blocks are interconnected by two ø 40 mm Swiss Gewi bars made of B500B steel. Fig. 9 provides front and top views of the V-SE vault, illustrating the concrete blocks and chains used. It is important to note that, as shown in [18], SE can be reinforced with steel bars, especially in the taut area, to enhance strength and toughness. However, in this instance, an electro-welded mesh ø6 100 × 100 mm was embedded into the V-SE vault's intrados solely just to reproduce a common practice in the field. This mesh helps maintain the correct shape of the vault and facilitates the attachment of a lightweight and flexible plywood formwork against which the material is projected. The concrete reinforcement cover is 4 cm thick, and the mesh used is made of B500B steel. The manufacturing of the V-ER and V-RM vaults took place within the laboratory of the Haute Ecole d'Ingénierie et de Gestion du Canton de Vaud (HEIG-VD), as depicted in Fig. 10. They underwent one month of curing before testing under controlled conditions at a temperature of 20 ± 2 °C and a relative humidity of 55 ± 10%. Inside the laboratory, climatic control systems were utilized to maintain temperatures and relative humidity within the specified ranges. In contrast, the V-SE vault's fabrication occurred outdoors during the winter season due to space constraints and dust generation. Following curing outside the laboratory, the vault was moved indoors and subjected to controlled laboratory conditions (20 ± 2 °C temperature and 55 ± 10% relative humidity) until testing. Fig. 11 illustrates the different stages of the V-SE vault construction process.

Table 4

Vaults geometric parameters.

		V-ER	V-SE	V-RM
Total length of the vault	L_V	4.16 m	4.16 m	4.16 m
Shorter distance between the two vault supports	L_P	4.00 m	4.00 m	4.00 m
Width	b	2.20 m	2.20 m	2.20 m
Thickness	h	0.115 m	0.20 m	0.12 m
Radius of the curved line	R_V	4.25 m	4.25 m	4.25 m

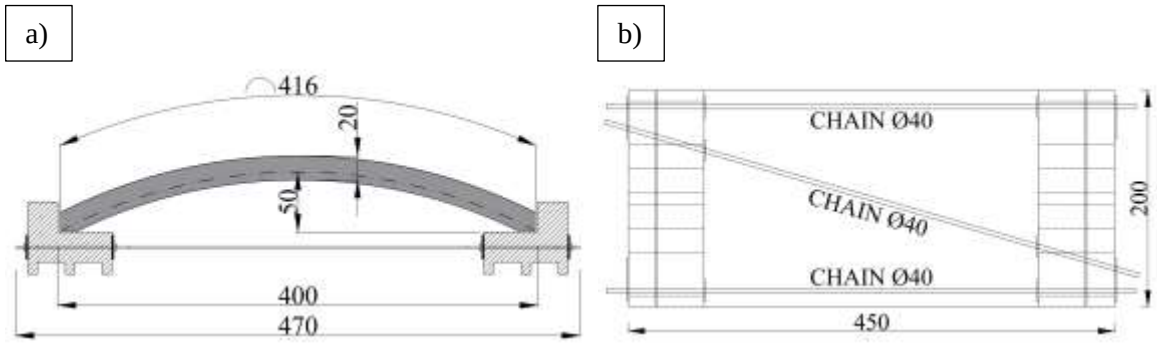

Fig. 9. V-SE vault: a) 2D frontal representation (dimensions in centimeters), b) 2D plan representation (dimension in centimeters).

Fig. 10. Vault fabrication: a) V-ER, b) V-RM.

Fig. 11. V-SE: a) formwork, b) projection process, c) after projection, d) after curing.

4.2. Vault tests

4.2.1. Instrumentation setup

To gain a thorough understanding of the mechanical response of a full-scale vault, various loading configurations were examined. The first case (C1) analyzed the elastic response when a distributed service load was applied. The second case (C2) focused on the elastic response with a distributed asymmetric load applied to one half of the vault. The third case (C3) examined the mechanical response as an asymmetric linear load which is increased until complete collapse. For deflection measurements, five LVDTs were placed on both sides of the vault being tested, positioned at a distance of $L_P/6 = 66.67$ cm from each other, as shown in Fig. 12. Additional LVDTs were positioned at the base of the concrete blocks to measure slippage relative to the chains and assess overall horizontal saddle displacement at the base of the concrete blocks, as illustrated in Fig. 12b. To capture the ductile behavior of the V-SE

vault, during C3 loading setup, one half of the V-SE vault was monitored using a stereoscopic photogrammetry system until failure, as seen in Fig. 13a. Photogrammetry technology allowed for the creation of 3D point clouds to monitor vertical displacements during the test and track the evolution of crack openings as well [37]. To compare the point clouds recorded at different times, an appropriate number of reference points was applied to the portion of the V-SE vault under investigation, as depicted in Fig. 13b.

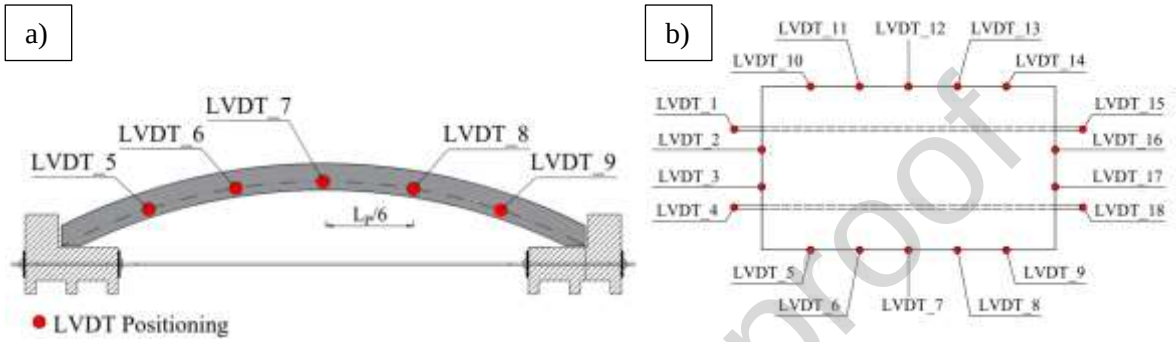

Fig. 12. LVDTs setup: a) one side of the vault, b) 2D plan representation.

Fig. 13. a) Photogrammetry instrument setup, b) Reference points disposition in the portion of V-SE vault analyzed via photogrammetry technology.

4.2.2. Elastic test – Symmetrical (C1) and Asymmetrical (C2) loadings

To assess the elastic response of a SE-V vault, a distributed load is applied by positioning eight 1000-liter IBC tanks on the vault. The water level filled in each tank corresponds to a load of 3.20 kN/m^2, evenly distributed across the top surface of the vault. This load magnitude has been chosen to represent typical service loads. Both strength and stiffness of the SE-V vault are determined based on the experimental findings detailed in Section 3. Expanded polystyrene layers with adjusted geometry are used to evenly distribute the load on the vault extrados, as shown in Fig. 14. The load is maintained until the local deflection, measured by LVDTs, is less than 0.002mm within a 15-minute timeframe. Beyond this point, fluctuations associated with load stabilization are no longer present, thus indicating the onset of creep phenomena.

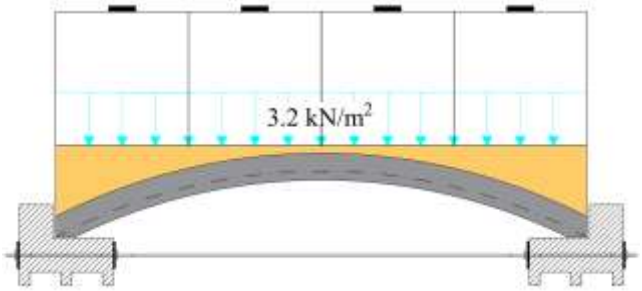

Fig. 14. Symmetrical loading layout (C1).

To examine the second load condition (C2), four out of the eight tanks are filled to create an asymmetrical surface load. The testing of the vaults involves tailored methodologies for each vault type to ensure optimal conditions. Specifically, for the V-ER vault, an asymmetric load is achieved by emptying sectors A and C, as shown in Fig. 15. Similarly, for the V-RM vault, an asymmetric load distribution is created by emptying sectors B and D, also depicted in Fig. 15. For the V-SE vault, a different approach is used after the C1 test. Initially, all tanks are emptied, and then only those placed in zones A and C are subsequently filled. This approach enables the assessment of how the vaults respond to an asymmetric load distribution within the elastic range, as illustrated in Fig. 16. The load magnitude in C2 remains the same as in C1, i.e., 3.20 kN/m^2. As in C1, the load is maintained until the local deflection, measured by LVDTs, is less than 0.002 mm within a 15-minute timeframe, at which point the test is halted. Evaluating deformative behavior under asymmetric loading conditions is crucial because vaults are highly sensitive to asymmetries. Indeed, asymmetric loads or construction-related geometric irregularities can promote unpredictable stress states and, in turn, excess of deformation and premature damage of the vault. Additionally, the cracking mechanism is strongly influenced by the heterogeneity and variability in the properties of brick materials, which can also cause asymmetries.

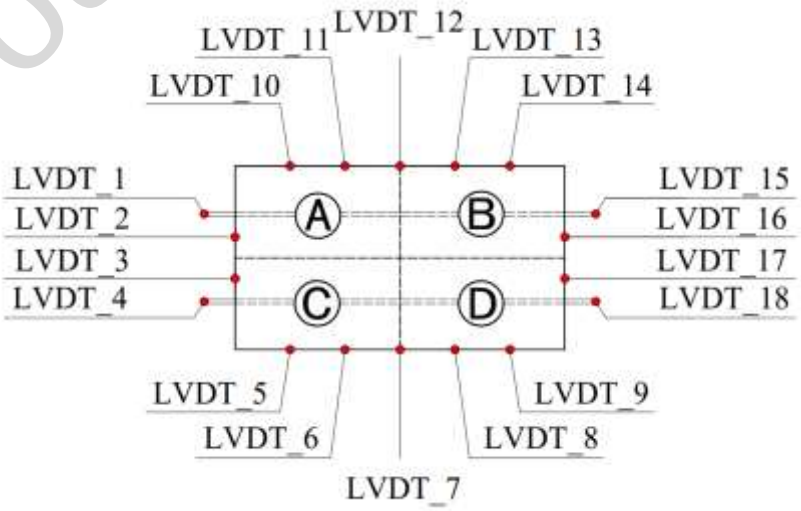

Fig. 15. Vault LVDT setup and section division in a 2D plan representation.

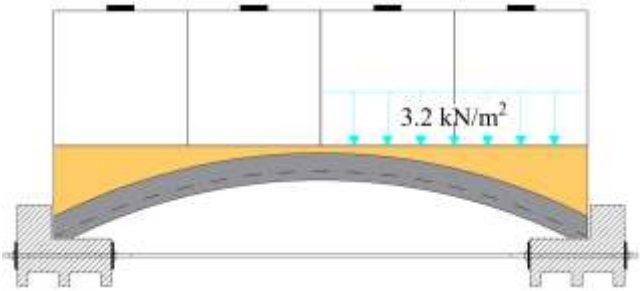

Fig. 16. Asymmetrical loading system (C2).

4.2.3. Rupture test – Distributed linear load (C3)

Following the tests based on the C1 and C2 loading configurations, a loading test (C3) is conducted, continuing until complete collapse of the vault. The IBC tanks are removed, and a prismatic concrete support is constructed on the extrados of the vault at $L_P/4$ to accommodate the steel beam upon which the actuators are placed. This support base allows for the application of a linear load on the extrados, as shown in Fig. 17. The load is applied using two 300 kN servo-hydraulic actuators, with a displacement control rate set at 0.005 mm/s. After the crack pattern stabilizes, the displacement rate is adjusted to 0.01 mm/s until complete failure occurs.

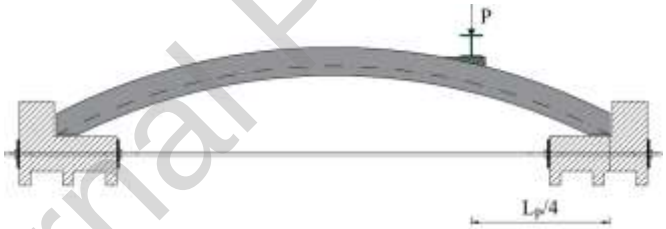

Fig. 17. Loading system (C3) to test the vault until collapse.

4.3. Modeling

A finite element (FE) model was created using the commercial software SCIA Engineering [38] for two main purposes: first, to establish a predictive model of the vaults' behavior under service loads, and second, to predict the ultimate bearing capacity of the vault under the C3 loading condition..

The FE model was constructed using curvilinear beam elements, as depicted in Fig. 18. In detail, the vault was discretized with curved 1D elements, each having a length of 0.01 m.

In the case study, chains are present at the base of the concrete blocks. These chains are modeled by incorporating a single equivalent chain to represent an equivalent stiffness, denoted as *K* (N/mm), as determined by Eqs. (4)-(5):

$$K = \frac{E_S\, A_{SC}}{l_s}(\cos\alpha)^2 + 2\,\frac{E_S\, A_{SC}}{l_s} \tag{4}$$

$$\alpha = \tan^{-1}\left(\frac{b_s}{l_s}\right) \tag{5}$$

where E_s is the elastic modulus of the steel chains (MPa), A_{sc} is the area of a single chain (mm²), l_s is the length of the horizontal chains (mm), b_s is the distance between the two horizontal chains (mm).

In the FE model, the concrete blocks at the base of the vaults only restrain translations, so ideal hinges are adopted to simulate the constraints.

Fig. 19 illustrates the load patterns (C1) and (C2) considered in the study. It's worth noting that for the V-ER and V-RM vaults, after the C1 phase, four 1000 *l* IBC tanks were emptied in specific zones, as explained in Section 4.2.2, transitioning to the C2 configuration. Additionally, it is assumed that the deformed configuration (due to the C1 load) can be considered undeformed in the case of C2 for V-ER and V-RM vaults. Small displacements at the base of the support concrete blocks have significant effects on the vertical displacements of the vault. Therefore, the model takes into account the displacement recorded by the LVDTs positioned at the base of the concrete blocks to accurately reproduce the loading condition.

For the asymmetrical line distributed load (C3), it is applied at a distance of $L_p/4$ from the hinge, simulating a load footprint of 30 cm on the top of the vault (vertical projection), as shown in Fig. 20a. Another load distribution is considered with an inclination of 45°, following specifications [39], until the middle line is reached, as shown in Fig. 20b. The mechanical parameters used in the FE models have been calibrated based on the experimental results presented in Section 3, and these parameters are summarized in Table 5.

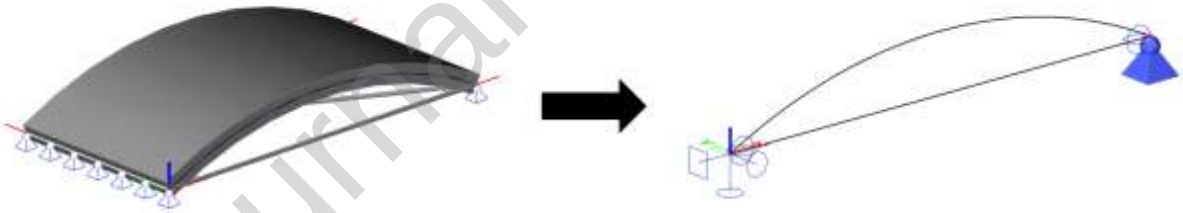

Fig. 18. Vault FE model using 1D "beam" elements.

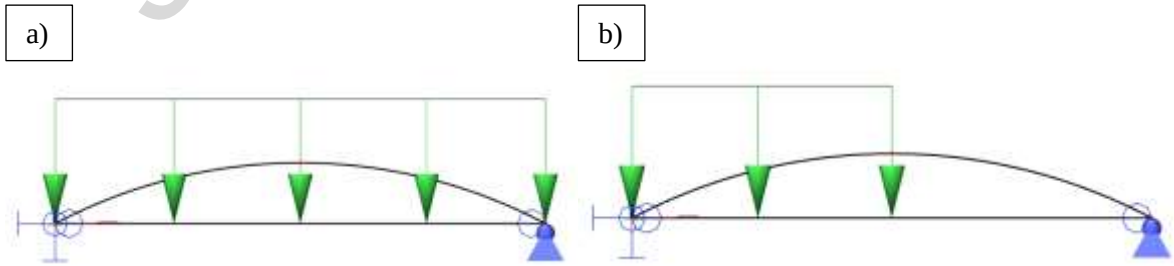

Fig. 19. FE model load case: a) C1, b) C2.

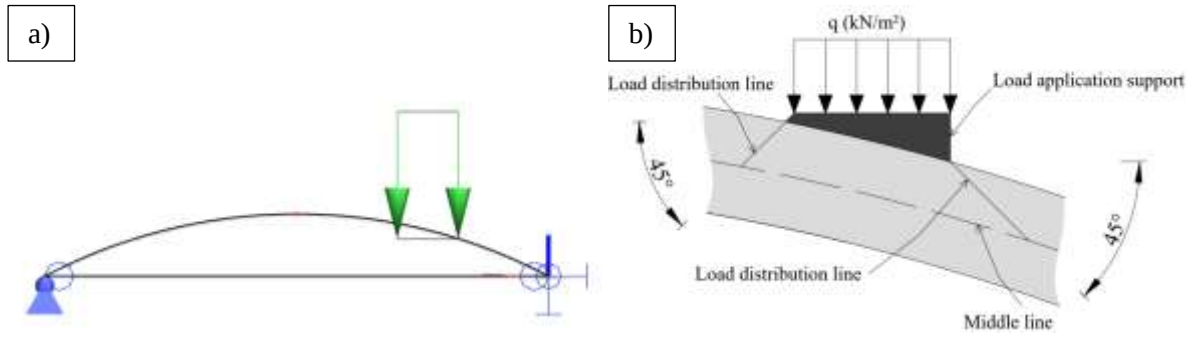

Fig. 20. a) Asymmetrical load applied on the vertical projection, b) Load diffusion at 45°.

Table 5
ER, SE, RM vaults: calibration of the parameters for the modelling.

Cases studied	EM (MPa)	$f_{c,max}$ (MPa)	f_t (MPa)	h (mm)	A_s (mm²)
V-ER	4962	6.51	2.6	115	-
V-RM	7640	7.67	3.41	120	-
V-SE	12998	10.9	2.04	200	791.68

EM: elastic modulus;
$f_{c,max}$: 28 day compressive strength;
f_t: tensile strength;
h: cross section height;
As: Area of the steel reinforcement.

The determination of the failure load involved conducting an incremental loading analysis. Starting from a baseline load, the applied load magnitude was gradually increased while continuously monitoring the distribution and magnitude of stresses. Failure was defined by reaching a critical threshold of stress levels, which was assessed through the axial force – bending moment interaction domain of the vault cross sections. This assessment was based on mean values for each material studied in Section 3.

For the V-ER and V-RM vaults, the behavior of the cross sections was described using a linear stress-strain relationship. In contrast, a parabola-rectangle relationship was adopted for the cross sections of the SE vault, based on prior studies [18,40]. The steel chains of the V-SE vaults were modeled with a classical elastic-perfectly plastic stress-strain relationship. It was assumed perfect adhesion between the steel and SE materials.

5. Results and discussion

5.1. Elastic test – Symmetrical (C1) and Asymmetrical load (C2)

Figs. 21-23 display the results obtained from the elastic tests conducted on the V-ER, V-SE, and V-RM vaults under the loading conditions (C1, C2) outlined in Section 4.2.2. During C1, the operational load induces a general deflection across the entire vault. However, this deflection is not symmetrical in both the transverse zones (A-C and B-D) and longitudinal directions (A-B and C-D), as shown in Figs. 21-23. This asymmetry can be attributed to geometric imperfections on the extrados surface of the vaults,

where the load is not evenly distributed, as illustrated in Fig. 24. Additionally, material heterogeneity may contribute to this behavior.

The same observations apply to C2, where an asymmetric surfacing load is applied. Negative values in Figs. 21-23 indicate a downward deflection. It is worth noting that, for the sake of clarity, LVDT_6 data related to the V-SE vault were not consistently acquired and have been excluded from the graph in Fig. 22 for the C2 load condition.

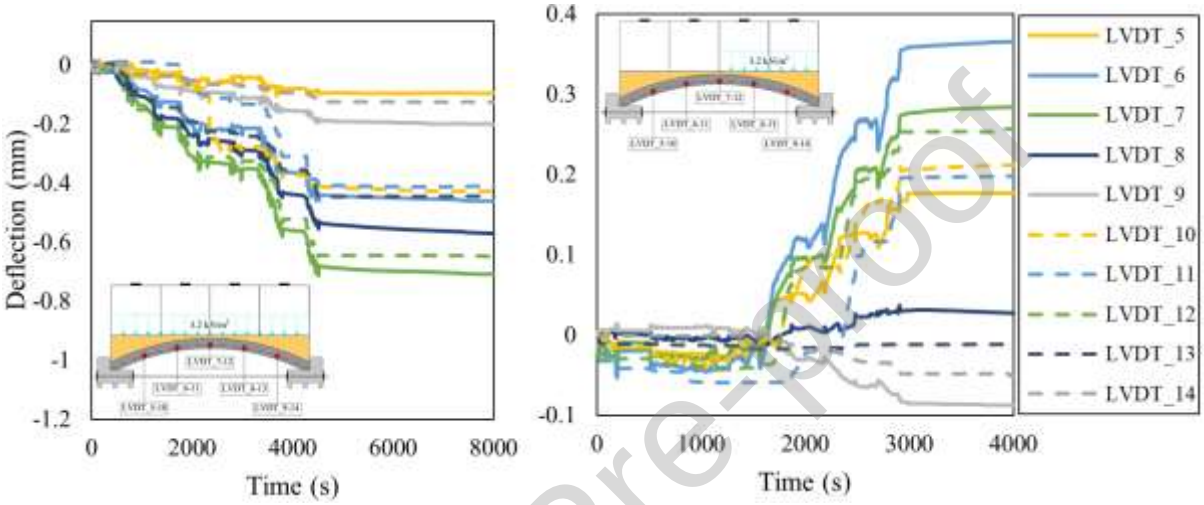

Fig. 21. Evolution of the deflection along time for V_ER for symmetrical and asymmetrical load conditions (C1 and C2).

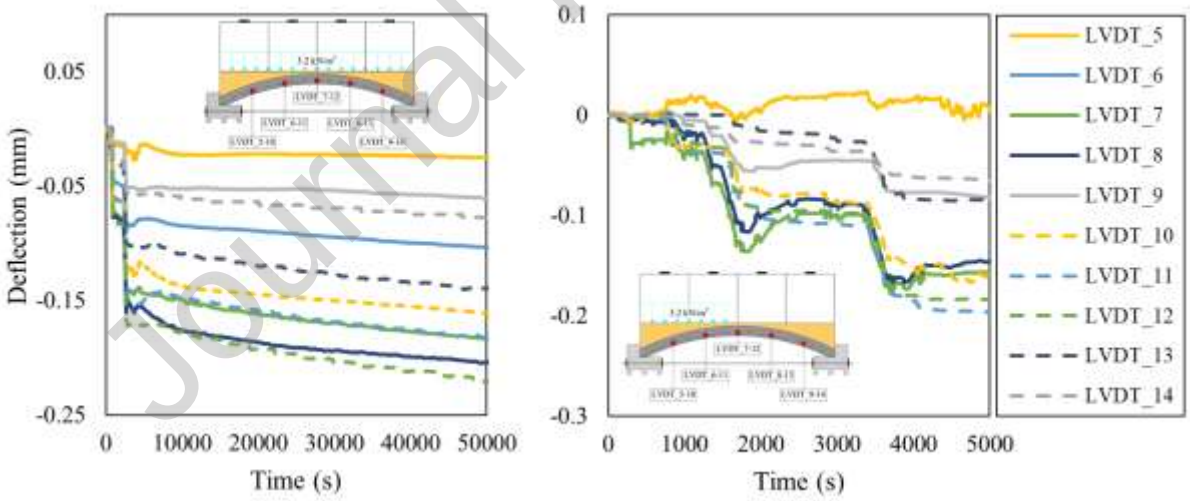

Fig. 22. Evolution of the deflection along time for V_SE for symmetrical and asymmetrical load conditions (C1 and C2).

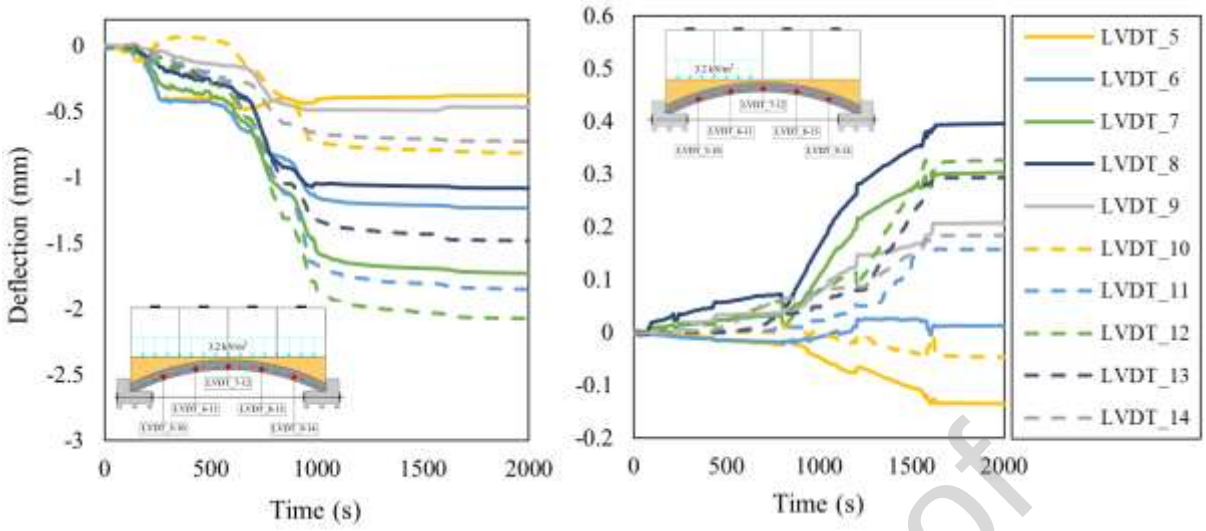

Fig. 23. Evolution of the deflection along time for V_RM vault for symmetrical and asymmetrical load conditions (C1 and C2).

Fig. 24. Loading patterns for the elastic test: a) V-ER vault, b) V-SE vault, c) V-RM vault.

Table 6 presents a comparison between experimental and FE values of vertical displacements for each vault under the C1 and C2 loading conditions. For example, "V-ER-C1" represents the experimental value under the C1 loading condition, while "V-ER-FEM-C1" indicates the results for the same load case provided by the FE model.

The experimental data represent average deflection values recorded by the LVDTs, accounting for inelastic deformations. Notably, the displacements observed in the V-RM vault are considerably higher than those in the V-ER vault, which, in turn, are higher than those in the V-SE vault. This pattern holds true for both C1 and C2 loading conditions, thus confirming the greater stiffness of the vault made of SE. As indicated by the data listed in Table 6 and depicted in Fig. 25, the more homogeneous the material, the smaller the difference between experimental and theoretical results. It is important to note that, despite the various sources of uncertainty that can affect the results, the relative errors between FE and experimental results in terms of vertical displacements are less than 20% for the V-SE vault and below 50% for all the vaults considered here. This underscores that, despite its simplicity, a linearly elastic analysis performed through a FE model based on beam-like elements allows predicting properly the order of magnitude of displacements in the elastic regime.

Table 6
Comparison between experimental and FE deflections at C1 and C2 points.

LVDT	V-ER-C1 (mm)	V-ER-FEM-C1 (mm)	V-ER-C2 (mm)	V-ER-FEM-C2 (mm)
5-10	-0.126	-0.259	0.190	0.559
6-11	-0.433	-0.474	0.282	0.637
7-12	-0.674	-0.559	0.270	0.216
8-13	-0.503	-0.474	-0.132	-0.273
9-14	-0.160	-0.259	-0.148	-0.365
LVDT	V-SE-C1 (mm)	V-SE-FEM-C1 (mm)	V-SE-C2 (mm)	V-SE-FEM-C2 (mm)
5-10	-0.095	-0.120	-0.089	-0.094
6-11	-0.148	-0.208	-0.190	-0.140
7-12	-0.210	-0.240	-0.175	-0.120
8-13	-0.177	-0.208	-0.124	-0.071
9-14	-0.072	-0.120	-0.06	-0.027
LVDT	V-RM-C1 (mm)	V-RM-FEM-C1 (mm)	V-RM-C2 (mm)	V-RM-FEM-C2 (mm)
5-10	-0.596	-0.61	-0.091	-0.179
6-11	-1.543	-1.06	0.085	-0.106
7-12	-1.900	-1.221	0.315	0.180
8-13	-1.281	-1.06	0.345	0.414
9-14	-0.596	-0.61	0.194	0.345

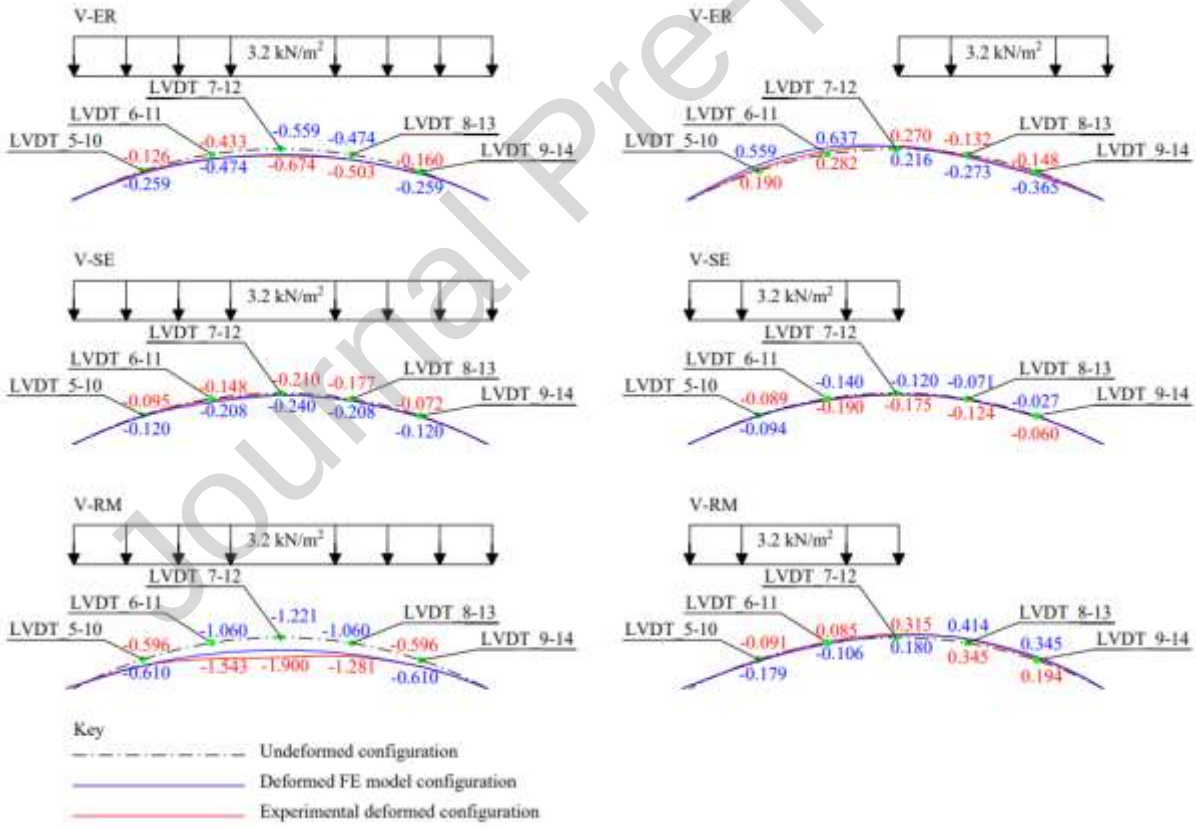

Fig. 25. Comparison between experimental and FE vertical displacements.

5.2. Collapse test – Distributed linear load (C3)

The crack patterns at the point of failure are depicted in Fig. 26 for all the considered vaults. In particular, for each vault, a crack occurred near the point of load application, followed by two additional cracks

near the supports, and another crack at the extrados, where the negative moment reaches its maximum (in absolute value). However, this latter crack is less pronounced in V-ER and V-RM vaults as compared to V-SE vaults. Additionally, in the case of V-ER and V-RM vaults, interfacial cracks also appeared in the mortar layer, leading to the separation of tiles. Minor transversal cracks occurred at the extrados (where the moment is negative) and at the intrados near the point of load application (where the moment is positive). These crack formations can be observed in Fig. 27, where they result in small fluctuations in the load-vs-time experimental data. It is important to note that the introduction of steel reinforcement at the intrados of the V-SE vault has enhanced its ductility in comparison to the other vaults.

For the V-SE vault, photogrammetry was employed to assess the evolution of deflection and crack opening as the load increased. The progressive crack opening was measured as the distance between two points within the point cloud using CloudeCompare software [41]. To obtain vertical deflection measurements at specific time points (for direct comparison with LVDT measurements), the point clouds were converted into raster elements, and the relevant images were analyzed using QGIS software [42]. The results related to the observed portions of the V-SE vault are presented in Fig. 28. Furthermore, additional cracks were observed in the tensile region (see Fig. 28) before the development of the second plastic hinge, as shown in Fig. 29. These images confirm that the formation of two plastic hinges, leading to the failure of the V-SE vault, follows the kinematic pattern depicted in Fig. 29. Results in terms of displacement-time and load-time curves during the failure test (C3) are presented in Figs. 27 and 30. It is worth noting that negative values indicate downward deflection. The LVDT_10 data related to the V-SE vault were not continuously acquired, and thus, they were removed from the graph in Fig. 30b.

The experimental results confirm that the V-SE vault can be effectively reinforced with steel, enhancing its ductility and making it a viable technology for constructing load-bearing vault-like structures.

In this phase, the FE simulations coupled with the normal force-bending moment interaction diagram, serves as a predictive model for assessing the failure load. The calibration of the FE models and interaction diagrams was carried out in accordance with the results presented in Section 3 and data from the Literature [10,18]. For the V-ER and V-RM vaults, the asymmetric linear load (C3) in the FE model is varied until complete failure. The load that triggers the formation of the first plastic hinge will be referred as "FVSE1." Therefore, the FE model for the V-SE vault was updated by introducing a hinge at the load application zone, as shown in Fig. 31. The load is then further increased until the formation of the second plastic hinge, i.e., when the sum of the stresses resulting from FVSE1 and the load increment in this new configuration are such to reach the failure domain's boundary. The sum of these two loads activates the kinematic mechanism for the V-SE vault.

The ultimate load-bearing capacities and the corresponding failure domains are presented in Fig. 32 and Table 7. A comparison between FE predictions and experimental results regarding failure load is also provided.

Fig. 26. Crack pattern at collapse for: a) V-ER, b) V-SE, c) V-RM vaults.

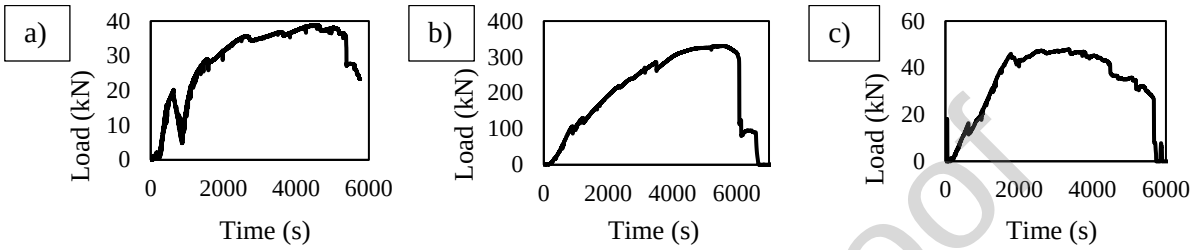

Fig. 27. Force – Time evolution during the rupture test (C3) for: a) V-ER, b) V-SE, c) V-RM vaults.

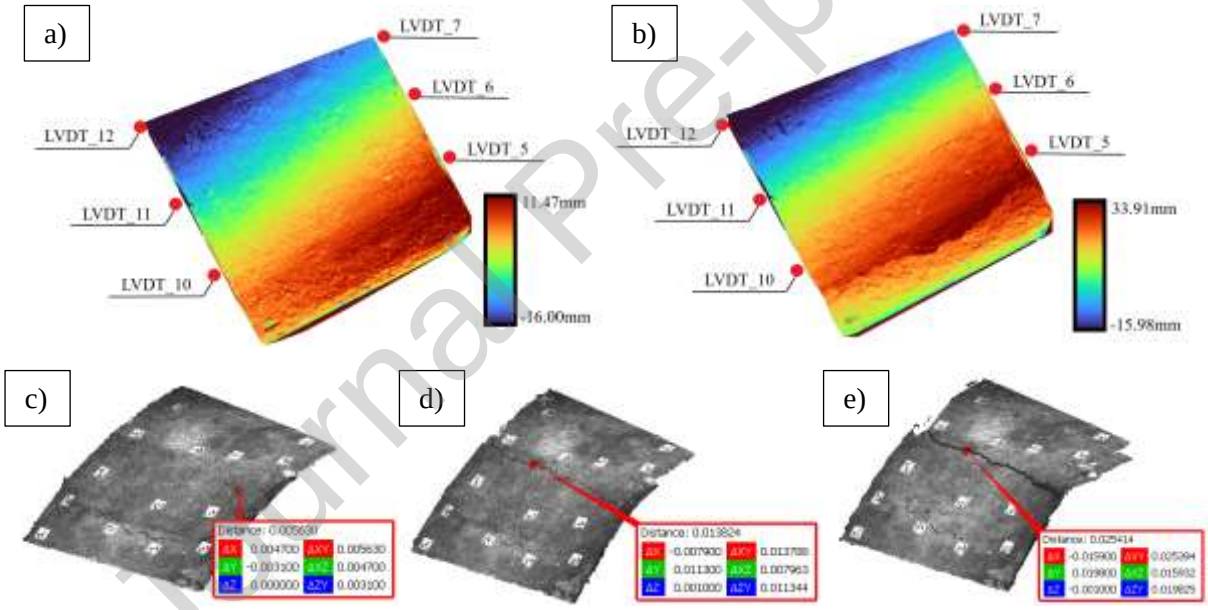

Fig. 28. Measurements provided by photogrammetry for V-SE vault: a) deflection at t = 5100 s, b) deflection at t = 6700 s, c) crack openings at t = 6700 s (dimensions in m), d) crack openings at t = 8200 s (dimensions in m), e) crack openings at t = 8550 s (dimensions in m).

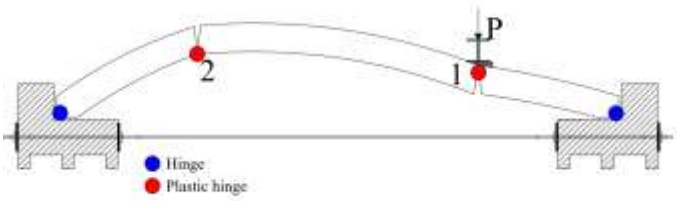

Fig. 29. V-SE vault: hinge constraints arrangement and progressive formation of plastic hinges until the complete failure.

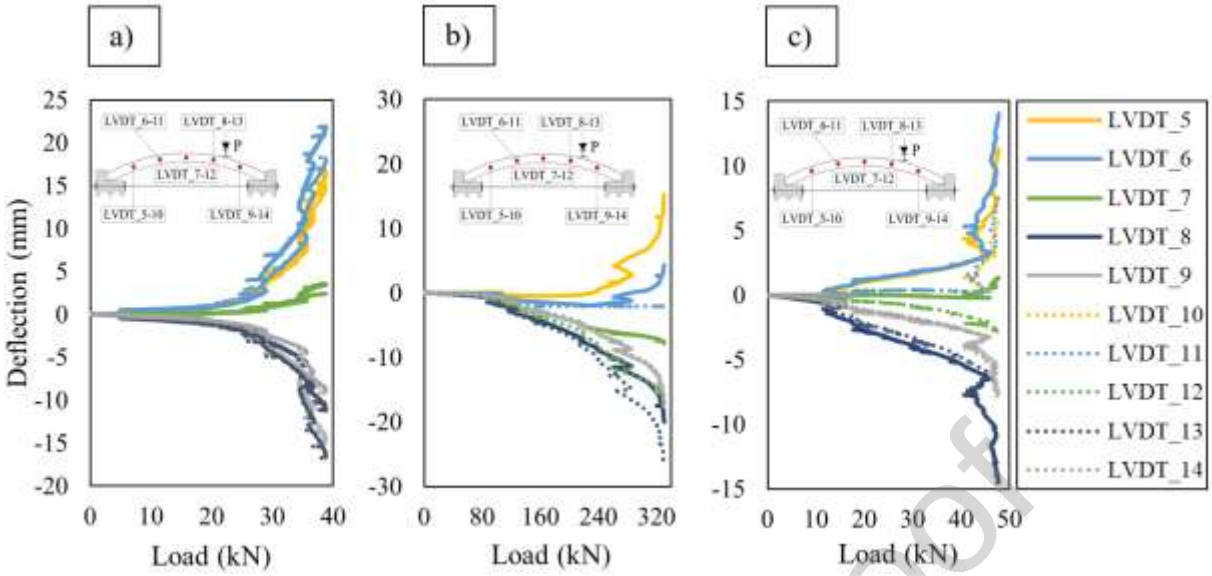

Fig. 30. Deflection – Load relationship during the collapse test for: a) V_ER, b) V_SE, c) V_RM V-SE vaults.

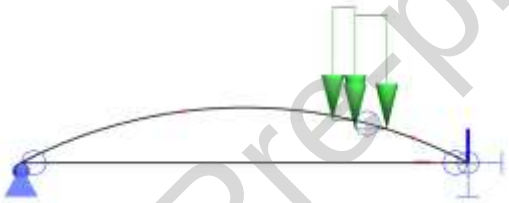

Fig. 31. FE model after the formation of the first plastic hinge in the V-SE vault.

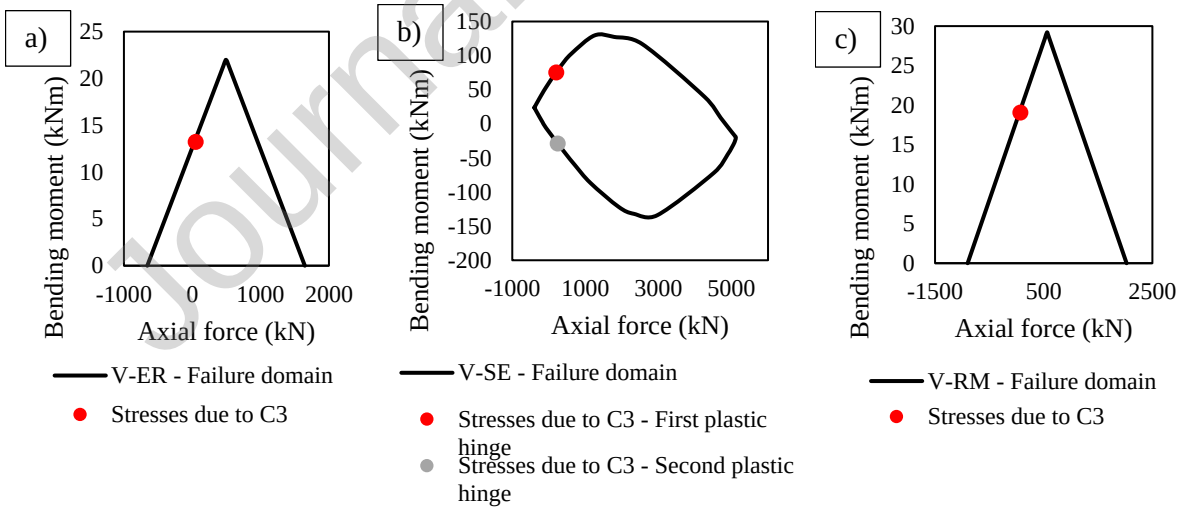

Fig. 32. Failure domain for: a) V-ER, b) V-SE, c) V-RM vaults.

Table 7
Comparison between the predicted and the experimental load failure in terms of load failure.

Cases studied	Predicted load failure (kN)	Experimental load failure (kN)	Percentage error (%)
V-ER	47	39	-20.51
V-SE	243	331	26.57
V-RM	63	48	-31.25

The V-SE vault outperforms the others significantly, with about 7 times the resistance of the V-RM vault and 8.5 times that of the V-ER vault. This finding suggests that reinforced SE is more akin to concrete than traditional brick techniques, due to its strength and structural similarities. This indicates the need for further testing, particularly focusing on comparisons with reinforced concrete.

The percentage differences between experimental and theoretical results, roughly around 30%, are deemed acceptable despite the simplifications made in the FE model, which do not account for the high heterogeneity of masonry materials. This simplified model is deemed suitable based on the conducted test. If significant asymmetries orthogonal to the vault's axis arise, then a 2D or 3D model would be essential. Otherwise, the simplified beam model suffices with commendable predictive capabilities.

These results lead to the conclusion that all three of the technologies used in this study are suitable for constructing load-bearing structures primarily subjected to compression. These findings carry significant implications for the construction industry, offering a robust basis for the adoption of steel-reinforced SE materials and the utilization of compressed earth bricks as sustainable alternatives to conventional construction materials. Moreover, they endorse the notion that a notable enhancement in the strength of SE can be realized by integrating a second steel mesh, identical in type and diameter to the one positioned at the bottom. This enhancement could be particularly pronounced when both meshes are interconnected and distanced by U-shaped steel bars placed at the sides of the vault structure.

6. Conclusions

In this study, full-scale vaults constructed using ER, reinforced SE, and RM layouts were investigated. The engineering properties specific to each layout were assessed through axial compression tests for walls, three-point bending tests for RM, and data obtained from the Literature.

Additionally, new experimental results regarding the mechanical behavior of SE vaults were obtained and compared with traditional technologies, both in the elastic domain and at collapse.

Based on the results obtained in this research, the following conclusions can be drawn:

1. The earth-based "eco" version of traditional rasilla (ER) provides a sustainable alternative for constructing classic Catalan vaults. Despite its lower strength and moderate mechanical properties, its adherence to FE predictive models is as effective as that of the traditional rasilla (RM). With established mechanical parameters, the structural behavior of vault elements made from ER can be accurately predicted, positioning it as a viable sustainable option.
2. The SE (shot-earth) exhibits slightly higher basic mechanical performance compared to the other technologies investigated, with a compressive strength margin of 30%. Notably, when reinforced with meshes, SE vaults achieve collapse resistances 7 to 8.5 times greater than those of the ER (raw-earth) and RM (terracotta) vaults tested, thus demonstrating improved performances in terms of strength and ductility as well.

3. The combined use of FE models and axial force-bending moment interaction diagrams enables the prediction of failure loads for earth-based vaulted structures with acceptable accuracy.

These findings hold significant implications for the construction industry, providing a robust basis for adopting steel-reinforced SE materials and compressed earth bricks as sustainable alternatives to conventional construction materials. In addition, this reveals the potential for reinforced SE to extend its application beyond compression-loaded elements, encompassing flexural components like slabs and beams.

The experimental results suggest that SE performances resemble more those of concrete rather than those of brick materials. The presence of reinforcement has demonstrated its effectiveness in enhancing both strength and ductility, as evidenced by the development of plastic hinges. Hence, future studies will focus on comparing concrete and SE technologies to develop tailored predictive models for SE, building upon existing concrete models.

Declaration of Competing Interest

The authors declare that they have no known competing financial interests or personal relationships that could have appeared to influence the work reported in this paper.

Acknowledgments

Financial support from the HES-SO in the framework of the projects « NextEarthBuild – Une nouvelle génération d'éco-construction en terre d'excavation recycle – n° 98528 » and « EcoAbri – Construction d'un abri témoin en terre d'excavation et autres matériaux écologiques et indigènes en vue de la réalisation ultérieure d'un espace de rangement non chauffé – n° 108222 » is gratefully acknowledged. Financial support from Innosuisse in the framework of the Project « Innosuisse – Shotearth : a sustainable excavated-soil based building material – n° 52127.1 IP-EE » is gratefully acknowledged as well. LL gratefully acknowledges financial support from the Italian Ministry of University and Research (MUR) in the framework of the project PRIN 2020 ‘‘Opportunities and challenges of nanotechnology in advanced and green construction materials’’ (prot. 2020EBLPLS; CUP: E95F20002390001). AMT gratefully acknowledges financial support from the Italian Ministry of University and Research (MUR) in the framework of the project PRIN 2022 "New eco-friendly building materials inspired by ancient constructions" (prot. 2022Y2RHHT; CUP E53D23003900006) and project FISA-2022 "Earth-Tech" (code 00183; CUP: E93C24000250001).

References

[1] G. Duarte, N. Brown, A. Memari, J.P. Duarte, Learning from historical structures under compression for concrete 3D printing construction, Journal of Building Engineering 43 (2021) 103009. https://doi.org/10.1016/j.jobe.2021.103009.

[2] S.B. Fletcher, A History of Architecture on the Comparative Method, 17th Edition, Seventeenth Edition, Charles Scribner’s Sons, 1967.

[3] S. Timoshenko, S. Woinowsky-Krieger, Theory of Plates and Shells, McGraw-Hill, 1959.
[4] M. Hejazi, B. Hejazi, S. Hejazi, Evolution of persian traditional architecture through the history, Journal of Architecture and Urbanism 39 (2015) 188–207. https://doi.org/10.3846/20297955.2015.1088415.
[5] C. Costa, Â. Cerqueira, F. Rocha, A. Velosa, The sustainability of adobe construction: past to future, International Journal of Architectural Heritage 13 (2019) 639–647. https://doi.org/10.1080/15583058.2018.1459954.
[6] Syrian Beehive Houses – EARTH ARCHITECTURE, (2009). https://eartharchitecture.org/?p=571 (accessed June 21, 2023).
[7] Ṭāq Kisrā | ancient palace, Iraq | Britannica, (2023). https://www.britannica.com/place/Taq-Kisra (accessed June 21, 2023).
[8] S. Benfratello, G. Caiozzo, M. D'Avenia, L. Palizzolo, Tradition and modernity of catalan vaults: historical and structural analysis, in: 2012. https://www.semanticscholar.org/paper/TRADITION-AND-MODERNITY-OF-CATALAN-VAULTS%3A-AND-Benfratello-Caiozzo/a3b39158fe207acab7d02da93c8c82a342d82c07 (accessed June 21, 2023).
[9] B. Torres, E. Bertolesi, J.J. Moragues, P.A. Calderón, J.M. Adam, Experimental investigation of a full-scale timbrel masonry cross vault subjected to vertical settlement, Construction and Building Materials 221 (2019) 421–432. https://doi.org/10.1016/j.conbuildmat.2019.06.015.
[10] V. Savino, M. Franciosi, M. Viviani, Engineering and analyses of a novel Catalan vault, Engineering Failure Analysis 143 (2023) 106841. https://doi.org/10.1016/j.engfailanal.2022.106841.
[11] S. Adriaenssens, P. Block, D. Veenendaal, C. Williams, eds., Shell Structures for Architecture, 0 ed., Routledge, 2014. https://doi.org/10.4324/9781315849270.
[12] J. Heyman, The stone skeleton, International Journal of Solids and Structures 2 (1966) 249–279. https://doi.org/10.1016/0020-7683(66)90018-7.
[13] M. Lévy, Sur l'équilibre élastique d'une plaque rectangulaire, Comptes rendus l'Académie des Sci. Paris 129 (1966) 249–256.
[14] E. Milani, G. Milani, A. Tralli, Limit analysis of masonry vaults by means of curved shell finite elements and homogenization, International Journal of Solids and Structures 45 (2008) 5258–5288. https://doi.org/10.1016/j.ijsolstr.2008.05.019.
[15] D. López López, T. Van Mele, P. Block, Tile vaulting in the 21st century, Informes de La Construcción 68 (2016) e162.
[16] S. Vantadori, A. Żak, \Lukasz Sadowski, C. Ronchei, D. Scorza, A. Zanichelli, M. Viviani, Microstructural, chemical and physical characterisation of the Shot-Earth 772, Construction and Building Materials 341 (2022) 127766.
[17] A. D'Alessandro, A. Meoni, V. Savino, M. Viviani, F. Ubertini, New self-sensing shot-earth cement-composites for smart and sustainable constructions: experimental validation on a full-scale vault, Proceedings of 6th Workshop on The New Boundaries of Structural Concrete 2022 University of Salento - ACI Italy Chapter (2022) 151–160.
[18] A. Curto, L. Lanzoni, A.M. Tarantino, M. Viviani, Shot-earth for sustainable constructions, Construction and Building Materials 239 (2020) 117775.
[19] M. Bacciocchi, V. Savino, L. Lanzoni, A.M. Tarantino, M. Viviani, Multi-phase homogenization procedure for estimating the mechanical properties of shot-earth materials, Composite Structures 295 (2022) 115799. https://doi.org/10.1016/j.compstruct.2022.115799.
[20] M. Franciosi, V. Savino, L. Lanzoni, A.M. Tarantino, M. Viviani, Changing the approach to sustainable constructions: An adaptive mix-design calibration process for earth composite materials, Composite Structures (2023) 117143. https://doi.org/10.1016/j.compstruct.2023.117143.
[21] A.M. Tarantino, F. Cotana, M. Viviani, Shot-Earth for an Eco-friendly and Human-Comfortable Construction Industry, Springer Nature Switzerland, 2023.
[22] B.V. Venkatarama Reddy, P. Prasanna Kumar, Embodied energy in cement stabilised rammed earth walls, Energy and Buildings 42 (2010) 380–385. https://doi.org/10.1016/j.enbuild.2009.10.005.

[23] Q.-B. Bui, J.-C. Morel, S. Hans, P. Walker, Effect of moisture content on the mechanical characteristics of rammed earth, Construction and Building Materials 54 (2014) 163–169. https://doi.org/10.1016/j.conbuildmat.2013.12.067.
[24] P. Walker, ed., Rammed earth: design and construction guidelines, BRE Bookshop, Watford, 2005.
[25] L.M. Gil-Martín, M.A. Fernández-Ruiz, E. Hernández-Montes, Mechanical characterization and elastic stiffness degradation of unstabilized rammed earth, Journal of Building Engineering 56 (2022) 104805. https://doi.org/10.1016/j.jobe.2022.104805.
[26] Q.-B. Bui, J.-C. Morel, Assessing the anisotropy of rammed earth, Construction and Building Materials 23 (2009) 3005–3011. https://doi.org/10.1016/j.conbuildmat.2009.04.011.
[27] V. Toufigh, E. Kianfar, The effects of stabilizers on the thermal and the mechanical properties of rammed earth at various humidities and their environmental impacts, Construction and Building Materials 200 (2019) 616–629. https://doi.org/10.1016/j.conbuildmat.2018.12.050.
[28] R. El-Nabouch, Q.-B. Bui, O. Plé, P. Perrotin, Assessing the in-plane seismic performance of rammed earth walls by using horizontal loading tests, Engineering Structures 145 (2017) 153–161. https://doi.org/10.1016/j.engstruct.2017.05.027.
[29] L. Miccoli, U. Müller, P. Fontana, Mechanical behaviour of earthen materials: A comparison between earth block masonry, rammed earth and cob, Construction and Building Materials 61 (2014) 327–339. https://doi.org/10.1016/j.conbuildmat.2014.03.009.
[30] G. Castori, A. Borri, M. Corradi, A new method for strengthening tiled vaults: "Reinforced Catalan vaulting," 2014.
[31] CEN, EN 12620:2002+A1:2008. Aggregates for concrete, Brussels, Belgium: CEN, 2008.
[32] CEN, EN 197-1:2011 Cement - Part 1: Composition, specification and conformity criteria for common cements, Brussels, Belgium: CEN, 2011.
[33] UNI Ente Italiano di Normazione, UNI EN 771-1:2011, 2011.
[34] J. Salirrosas, G. Silva, S. Kim, J. Nakamatsu, B. Bertolotti, R. Aguilar, Mechanical Characterization of a Masonry System Made of Alkaline Activated Pozzolana Blocks, MSF 1007 (2020) 111–117. https://doi.org/10.4028/www.scientific.net/MSF.1007.111.
[35] T. Li, M. Deng, Y. Ma, Y. Zhang, Study on axial compressive performance of HDC-masonry composite elements, Construction and Building Materials 304 (2021) 124593. https://doi.org/10.1016/j.conbuildmat.2021.124593.
[36] CEN, EN 12390-5:2019 Testing hardened concrete - Part 5: flexural strength of test specimens, Brussels, Belgium: CEN, 2019.
[37] S. Nishiyama, N. Minakata, T. Kikuchi, T. Yano, Improved digital photogrammetry technique for crack monitoring, Advanced Engineering Informatics 29 (2015) 851–858. https://doi.org/10.1016/j.aei.2015.05.005.
[38] SCIA Engineer 21.1, (2023). https://www.scia.net/fr/scia-engineer (accessed May 3, 2023).
[39] Ministero delle Infrastrutture e dei Trasporti, Norme tecniche per le costruzioni (NTC 2018), Roma: Gazzetta ufficiale, 2018.
[40] V. Savino, M. Franciosi, L. Lanzoni, A.M. Tarantino, M. Viviani, Shot-Earth: A Material for Structural Engineering, in: A.M. Tarantino, F. Cotana, M. Viviani (Eds.), Shot-Earth for an Eco-Friendly and Human-Comfortable Construction Industry, Springer Nature Switzerland, Cham, 2023: pp. 115–132. https://doi.org/10.1007/978-3-031-23507-8_7.
[41] CloudCompare, (2023). https://www.danielgm.net/cc/release/ (accessed June 22, 2023).
[42] QGIS 3.30.3, (2023). https://www.qgis.org/it/site/ (accessed June 22, 2023).

CONFLICT OF INTEREST

The authors declare that the present work has been realized in compliance with the Ethical Standards.

This study was funded by the aforementioned grant only.

Conflict of Interest: The authors declare that they have no conflict of interest.

HIGHLIGHTS

- Earth-based materials are employed to realize 4-meter span vault-like structures
- Shot-earth, “ecorasilla” masonry, and “rasilla terracotta” masonry technologies have been compared
- Basic mechanical properties of materials have been experimentally assessed
- Elastic response and ultimate strength of three full-scale vaults have been investigated
- FE simulations have been performed to predict the failure domain